Analysis of Galileo IOV + FOC signals and E5 RTK performance

Zaminpardaz, Safoora; Teunissen, Peter J.G.

DOI
10.1007/s10291-017-0659-9

Publication date
2017

Document Version
Final published version

Published in
GPS Solutions (online)

GPS Solut (2017) 21:1855–1870
DOI 10.1007/s10291-017-0659-9

ORIGINAL ARTICLE

Analysis of Galileo IOV + FOC signals and E5 RTK performance

Safoora Zaminpardaz[1] · **Peter J. G. Teunissen**[1,2]

Received: 14 July 2017 / Accepted: 11 August 2017 / Published online: 29 August 2017

Abstract The current Galileo constellation in April 2017 comprises both in-orbit validation and full operational capability satellites transmitting signals on five frequencies, i.e., E1, E5a, E5b, E5, and E6. We analyze the power, multipath and noise of these signals using the data collected by four short baselines of various lengths and receiver/antenna types in Perth, Australia, as well as the Netherlands. In our analysis, the Galileo signals, except E5, show different relative noise and multipath performance for different receiver/antenna types. The E5 signal, with a weak dependency on the type of receiver/antenna, shows a significantly lower level of multipath and noise with respect to the other signals. Estimations of the E5 code standard deviation based on the data of each of the mentioned baselines gives a value of about 6 cm, which is further reduced to about 1 cm once the data are corrected for multipath. Due to the superior stochastic properties of E5 signal compared to the other Galileo signals, we further analyze the short-baseline real-time kinematic performance of the Galileo standalone E5 observations. Our findings confirm that the Galileo E5 data, if corrected for the multipath effect, can make (almost) instantaneous ambiguity resolution feasible already based on the current constellation.

✉ Safoora Zaminpardaz
safoora.zaminpardaz@postgrad.curtin.edu.au

[1] GNSS Research Centre, Curtin University, GPO Box U1987, Perth, WA 6845, Australia

[2] Department of Geoscience and Remote Sensing, PO Box 5048, 2600 GA Delft, The Netherlands

Keywords Galileo · IOV · FOC · E5AltBOC · Signal power · Multipath · Noise characteristics · Integer ambiguity resolution · RTK

Introduction

Galileo, Europe's global navigation satellite system, has been under development through the collaboration of the European Commission (EC) and the European Space Agency (ESA), with the aim of providing highly accurate global positioning services (ESA 2016). Upon validating the Galileo design, two experimental Galileo in-orbit validation element (GIOVE) satellites, i.e., GIOVE-A and -B, were launched in 2005 and 2008, respectively. These satellites were put into orbit with the purpose of characterizing the performance of the novel Galileo signals and were later on decommissioned in 2012. The last two phases of the Galileo program are the in-orbit validation (IOV) phase and the full operational capability (FOC) phase. The former was planned to conduct the initial validation of the Galileo system based on four satellites and became finalized by 2014, while the latter is still ongoing to realize the fully operational system such that a minimum of four satellites is always visible at any location (http://www.esa.int/).

The full constellation of Galileo will comprise 24 satellites plus at most six spares, expected to be realized by 2020. They orbit in three medium earth orbit (MEO) planes, at an altitude of 23,222 km and with an inclination angle of 56° with respect to the equator (European Union 2015). The navigation signals of these satellites are transmitted on five frequencies E1, E5a, E5b, E5 and E6 (Table 1). Having alternative binary offset carrier (AltBOC) modulation, the Galileo E5 signal is a wideband

Table 1 Galileo frequencies and wavelengths

Signal	Carrier frequency (MHz)	Wavelength (cm)
E1	1575.420	19.03
E5a	1176.450	25.48
E5b	1207.140	24.83
E5	1191.795	25.15
E6	1278.750	23.44

signal consisting of two subcarriers, i.e., E5a and E5b, which can be tracked either as two independent BPSK(10) (binary phase shift keying) modulations at respective center frequencies of 1176.45 and 1207.14 MHz, or coherently as one signal centered at 1191.795 MHz, leading to the E5 signal (Simsky et al. 2006). Figure 1 illustrates how these frequencies are distributed with respect to the GPS L1, L2, and L5 frequencies.

The first analyses of the power, tracking noise and multipath performance of the Galileo signals based on the GIOVE-A and -B data were provided in Simsky et al. (2006, 2008a, b). Applying a geometry-free short- and zero-baseline analysis method to the measurements of GIOVE-A and -B, deBakker et al. (2009, 2012) analyzed the code and phase noise of E1 and E5a signals. Such zero-baseline analysis was also carried out by Cai et al. (2016) but on the basis of the four IOV satellites data at E1, E5a, E5b, and E5 frequencies. The code noise and the cross-correlation of these frequencies were assessed in Odijk et al. (2014).

Throughout different phases of the Galileo development, its data have been studied for a variety of GNSS applications either in Galileo-only mode or in Galileo plus other GNSSs mode. Examples of such studies are Langley et al. (2012), Tegedor et al. (2014, 2015), Afifi and El-Rabbany (2014), Cai et al. (2015), Li et al. (2015), Lou et al. (2016) and Guo et al. (2017), who presented the precise point positioning (PPP) results, Odijk et al. (2012, 2014) and Odolinski et al. (2015), who provided the short-baseline real-time kinematic (RTK) positioning results, Steigenberger et al. (2013), Cai et al. (2014), Gioia et al. (2015), Gaglione et al. (2015), Steigenberger and Montenbruck (2016), Pan et al. (2017) and Liu et al. (2017), who analyzed the single point positioning (SPP) performance, and Nadarajah et al. (2013, 2015) and Nadarajah and Teunissen (2014), who provided the attitude determination results.

The Galileo constellation in April 2017 consists of four IOV and 14 FOC satellites. The first two FOC satellites (PRNs E14 and E18) were launched in August 2014, albeit into wrong orbits (Hellemans 2014). By early 2015, they were moved to an improved orbit, such that the Galileo ground segment is now able to produce the navigation messages for these two satellites (GSA 2017). The fourth IOV satellite (PRN E20) experienced a power anomaly on May 27, 2014, which led to the shutdown of the E1 signal. Although this signal recovered within seconds, E5 and E6 signals suffered a permanent loss of power. Since then, PRN E20 has been flagged as 'NOT AVAILABLE' (Langley 2014). Among the 14 FOC satellites, four are newly launched and not operational yet. Therefore, in total, 13 Galileo satellites are currently providing data to the GNSS users. In the sequel, we refer to the constellation of these 13 satellites as the current Galileo constellation.

We analyze the multipath performance and the noise characteristics of all the five Galileo signals. For the former, the multipath combinations (Estey and Meertens 1999) are formed while for the latter use is made of the least-squares variance component estimation (LS-VCE) method (Teunissen and Amiri-Simkooei 2008; Amiri-Simkooei et al. 2009). These assessments are on the basis of the data of the current Galileo constellation–excluding E14 and E18–collected by baselines of various lengths and different receiver/antenna types in Perth, Australia, and in the Netherlands. This is the first time that the stochastic properties of the Galileo signals are assessed using both IOV and FOC satellites measurements. Our outcomes, in agreement with the previous studies (Simsky et al. 2006, 2008a), show a significantly lower level of noise and multipath for the E5 signal. This gives us the motivation to further investigate the E5 instantaneous RTK positioning

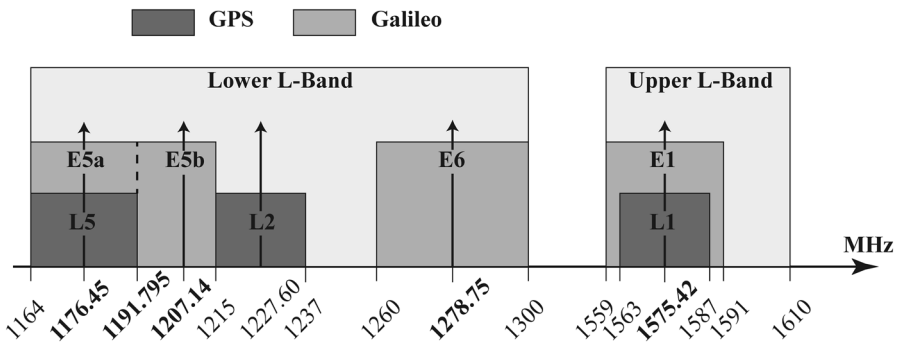

Fig. 1 Distribution of the Galileo frequencies versus GPS frequencies

performance. We then provide the Galileo standalone single-frequency E5-based RTK results. The understanding provided by such single-frequency analysis would also be useful for multifrequency analysis when integrating E5 with other frequencies. The detailed information on the data used in this study can be found in Table 2. Note the antennas used in this study do not offer, at the moment, the phase center calibrations for the Galileo E5, E5a, E5b and E6 signals. However, our analyses employing the short baselines of identical antennas are not affected by the lack of such calibrations (Mader 2002; EL-Hattab 2013).

Galileo signals characteristics

In this section, our aim is to characterize the Galileo signals stochastic properties. To do so, we investigate their power through C/N0 (carrier-to-noise density ratio), multipath performance through the code multipath combinations, and code and phase noise by means of the LS-VCE method.

Signal power

Shown in Fig. 2 are the graphs of the carrier-to-noise density ratio C/N0 of the Galileo signals with respect to the satellites elevation. The top two panels correspond to the measurements of station CUBS (Septentrio PolaRx5) while the bottom two panels correspond to those of station ADR2 (Leica GR50). The ground track of the Galileo constellation, except the two FOC satellites E14 and E18, repeats every 10 sidereal days, and therefore the Galileo satellites do not reach the whole range of elevations during one single day. Therefore, the C/N0 measurements were taken during a period of 10 days in 2017, which are days of year (DOYs) 54–63 in the case of CUBS, and DOYs 12–21 in the case of ADR2. For each station, the left panel corresponds to the FOC satellites while the right panel corresponds to the three IOV satellites. Each panel shows the average of the C/N0 data over elevation bins of 10°. Note that E6 signal is tracked only by Septentrio PolaRx5 receiver.

Comparing the C/N0 of Galileo signals, E5 shows the highest level of the carrier-to-noise density ratio for all the elevation angles, for both the FOC and IOV satellites and for both stations. In the case of CUBS, E1 and E5a have almost the same C/N0 for the range of elevations between 25° and 75°. For the elevation angles out of this range, E5a reaches a higher level of carrier-to-noise density ratio compared to the E1 particularly for the elevations higher than 75°. It can also be seen that the C/N0 of E1 experiences a drop at high elevations which was also reported in Simsky et al. (2006) using the space engineering antenna tracking the E1 data of GIOVE-A. The C/N0 of E6 lies above that of the E5b with almost the same difference for all the elevation angles. These two signals have a higher level of C/N0 with respect to the E1 and E5a. As to ADR2, the C/N0 signature of E5a coincides with that of E5b, both having higher levels than C/N0 of E1.

The observed carrier-to-noise density ratio depends on several factors such as the signal path, satellite hardware and antenna, receiving equipment including receiver, antenna, splitter and cable (Simsky et al. 2006; Hauschild

Table 2 Characteristics of the data set used for this study

Receiver—firmware Antenna—radome	Location	Station name
Septentrio PolaRx5—5.1.1 TRM 59800.00—SCIS	Curtin University, Perth, Australia	CUBS, CUCS SP01, UWA0
Leica GR50—4.00/7.001 LEIAR20 + S10—LEIM	The Netherlands	ADR2
Leica GR50—4.00/7.001 LEIAR25.R4—LEIT	The Netherlands	APEL
Data type	Galileo E1, E5a, E5b, E5, E6 (E6 is tracked only by Septentrio PolaRx5)	
Satellites	FOC (E01, E02, E08, E09, E22, E24, E26, E30) IOV (E11, E12, E19)	
Sampling interval	1 s (1 Hz)	
Baselines	CUBS-CUCS (6 m) CUBS-SP01 (350 m) ADR2-APEL (3.6 km) CUBS-UWA0 (7.9 km)	

All the antennas are survey grade and of choke-ring type

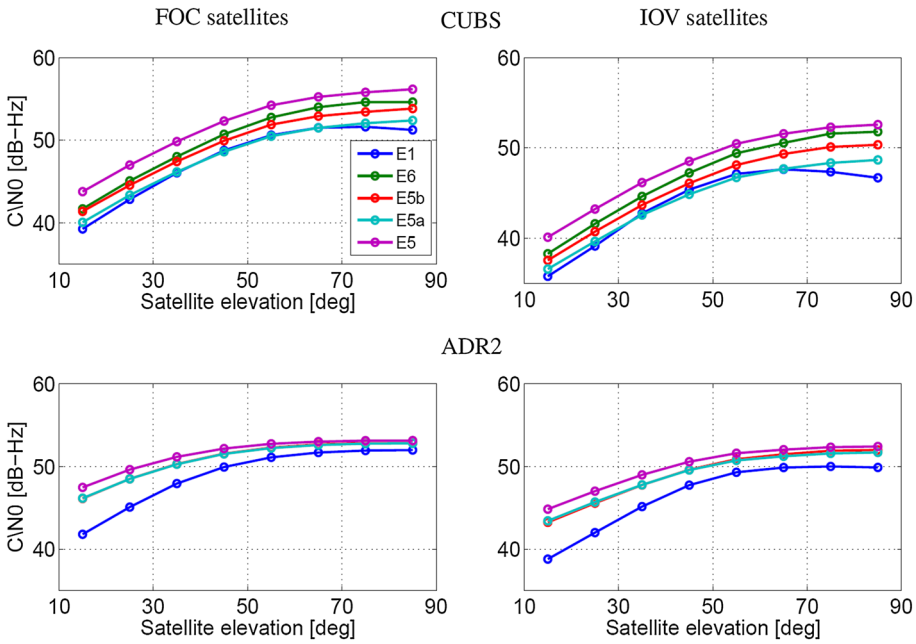

Fig. 2 Carrier-to-noise density ratio C/N0 of the Galileo signals on different frequencies as function of satellite elevation. The *top two panels* correspond to the measurements collected by station CUBS during DOYs 54-63 of 2017. The *bottom two panels* correspond to the measurements collected by station ADR2 during DOYs 12–21 of 2017. *Each panel* shows the average of C/N0 over elevation bins of 10°

et al. 2012). Such dependencies are well reflected in our observations in Fig. 2. The signals transmitted by the IOV satellites show a lower level of C/N0 in comparison with their FOC counterparts. This difference probably stems from the FOC and IOV satellites being different in transmit antenna patterns and transmit power levels. In addition, in 2014, following the fourth IOV (E20) sudden power loss and failure in transmission of the E5 and E6 signal, ESA imposed a reduction of 1.5 dB in the signal power of all the four IOV satellites (Langley 2014; Steigenberger and Montenbruck 2016). Beside the discrepancy between the IOV and FOC signals C/N0, we also noticed a difference between the C/N0 of IOV satellite pair E11/E12 and IOV satellite E19, being more pronounced in the case of Septentrio PolaRx5 receiver. According to our observations, the carrier-to-noise density ratio for E19 lies below that of the other two IOV satellites for the elevations higher than 60°.

Multipath performance

The Galileo code modulations are theoretically expected to suppress the long-delay multipath. In this sense, E5AltBOC not only outperforms the other signals, but it is also expected to have a high level of short-delay multipath rejection (Simsky et al. 2006, 2008a). In order to assess the multipath impact on Galileo signals, we form the code multipath combinations using the data collected by stations CUBS, SP01, and ADR2. The first two stations are equipped with the same receiver and antenna type, but have a different multipath environment (Table 2). The antennas deployed at all these three stations are of choke-ring type with low gain at low and negative elevation angles (Tranquilla et al. 1994). The code multipath combination is given as follows (Estey and Meertens 1999)

$$\begin{aligned}\eta^s_{r,j} &= p^s_{r,j} - \varphi^s_{r,j} + 2\frac{\lambda_j^2}{\lambda_i^2 - \lambda_j^2}\left(\varphi^s_{r,i} - \varphi^s_{r,j}\right) \\ &= \xi_{p^s_{r,j}} + c^s_{r,\{j,i\}} + \epsilon^s_{r,\{j,i\}},\end{aligned} \tag{1}$$

where $p^s_{r,j}$ and $\varphi^s_{r,j}$ denote the code and the phase observation from receiver r to satellite s on frequency j, respectively. λ_j is the wavelength of the frequency j. The code multipath combination $\eta^s_{r,j}$ is composed of code multipath, $\xi_{p^s_{r,j}}$, receiver/satellite hardware delays and integer-valued ambiguities on both frequency j and i, $c^s_{r,\{j,i\}}$, and the phase noise and multipath on both frequency j and i and the code noise on frequency j, $\epsilon^s_{r,\{j,i\}}$. The contribution of the multipath and noise of the phase observations $\varphi^s_{r,i}$ and $\varphi^s_{r,j}$ is amplified through the factor $\frac{2\lambda_j^2}{\lambda_i^2-\lambda_j^2}$ of which the absolute value in case j is set to E1, E5a, E5b, E5 and E6 can, respectively, reach up to 3.9 (i: E6), 78.2 (i: E5), 77.2 (i: E5), 76.2/79.2 (i: E5a/E5b) and 16.4 (i: E5b). The significance of this contribution for a given j is then governed by the choice of i and the relative magnitude of the multipath and noise of $p^s_{r,j}$ compared to those of $\varphi^s_{r,i}$ and $\varphi^s_{r,j}$. As will be discussed in the next subsection, the multipath and noise of the code observations of E1, E5a, E5b, and E6 frequencies are by far greater than those of the phase observations, such that when j is set to one of these frequencies, the contribution of the phase noise and multipath to (1) can practically be neglected for any choice of

i. As to E5, however, due to having centimeter-level code precision, one should avoid i: E5a/E5b since the phase noise and multipath contribution to (1) would be as large as code noise and multipath. In the following, for the cases j: E5a, E5b, E5 and E6, we set i: E1, and for the case j: E1, we set i: E5.

Figure 3 (Left) depicts the time series of the code multipath combination of the Galileo signals observed between station-satellite (from top to bottom) CUBS-E26 on DOY 118 of 2017, SP01-E26 on DOY 118 of 2017 and ADR2-E11 on DOY 21 of 2017. The satellite elevation is also shown as a gray dashed line. During the considered periods, the receiver/satellite hardware delays can be assumed constant over time, and since there was no loss of lock, the ambiguities are also constant over time. Therefore the term $c^s_{r,\{j,i\}}$ in (1) can be eliminated if the mean value of $\eta^s_{r,j}$ time series during the mentioned periods, denoted by $\bar{\eta}^s_{r,j}$, is subtracted from the $\eta^s_{r,j}$ time series. Shown in Fig. 3 (Left) are then the time series of $\eta^s_{r,j} - \bar{\eta}^s_{r,j}$. The differences in the multipath signature between these three panels stem from the differences in multipath environment and, in case of the bottom panel, the receiver/antenna type. As the satellite elevation decreases, the code multipath fluctuates more rapidly and with higher amplitudes. The Galileo signals in terms of the severity of this behavior can be ordered as E1 > E5a > E5b > E6 > E5 for the stations CUBS and SP01, and as E5a > E5b > E1 > E5 for the station ADR2. As to the E5, this behavior is mitigated considerably such that the E5 code multipath can be assumed to a large extent independent of the satellite elevation. The high performance of the E5 signal lies in its wide bandwidth and AltBOC modulation (Simsky et al. 2006; Diessongo et al. 2014).

Figure 3 (Right) provides the standard deviation of the code multipath combination over elevation bins of 10° for the Galileo signals. These graphs are obtained based on all the Galileo observations recorded by the corresponding stations during 10 days. The multipath performance of three signals E5a, E5b and E6 are similar to each other, poorer than E1 in the case of station ADR2 and better than E1 in the case of stations CUBS and SP01. The graphs corresponding with E5AltBOC shows a much flatter signature, revealing a small difference between high-elevation and low-elevation multipath for this signal. This observation is also consistent with the results presented by Simsky et al. (2006) based on the observations of GIOVE-A.

Measurement noise

The GNSS underlying observational model consists of two parts: functional model and stochastic model. The former describes how the parameters of interest, e.g., receiver-satellite range, ionospheric delay, receiver clock error, are related to the GNSS observations, while the latter describes the noise characteristics of the GNSS observables. In order to assess the noise characteristics of the Galileo signals, we employ the Galileo data of the short baselines CUBS-CUCS, CUBS-SP01, ADR2-APEL, and CUBS-UWA0 (Table 2), for which the differential ionospheric and tropospheric delays can be assumed negligible. With the covariance $C(.,.)$ operator, we consider the following stochastic model for the undifferenced code and phase observations on frequency j,

$$C\left(p^s_{r,j}, p^v_{u,j}\right) = \delta_{ru}\delta_{sv}\sigma^2_{p_j} w^s, \quad C\left(\varphi^s_{r,j}, \varphi^v_{u,j}\right) = \delta_{ru}\delta_{sv}\sigma^2_{\varphi_j} w^s, \quad C\left(p^s_{r,j}, \varphi^v_{u,j}\right) = 0, \tag{2}$$

where δ_{ru} is the Kronecker delta ($\delta_{ru} = 1$ for $r = u$ and zero otherwise), and δ_{sv} is defined likewise. w^s captures the satellite elevation dependency of the Galileo data through the exponential weighting function as

$$w^s = \left(1 + 10\exp\left(-\frac{\theta^s}{10}\right)\right)^{-2}, \tag{3}$$

where θ^s is the elevation of satellite s in degrees (Euler and Goad 1991). Note we have dropped the receiver index from θ^s and w^s since the elevation of satellite s can be assumed the same for the considered station pairs which are separated at a short distance. σ_{p_j} and σ_{φ_j} denote the zenith-referenced standard deviations of the undifferenced code and phase observations on frequency j, respectively.

Our aim is to find representative values for $\{\sigma_{p_j}, \sigma_{\varphi_j}\}(j = 1, \ldots, 5)$. To do so, we apply the LS-VCE method (Teunissen and Amiri-Simkooei 2008; Amiri-Simkooei et al. 2009) to the 1-s (1 Hz) double-differenced (DD) code and phase observations which are corrected for the DD ranges and, in case of phase observations, the integer DD ambiguities. The DD ranges were computed from the known receiver and satellite positions. Whereas the reference integer ambiguities were computed using the very strong multiepoch baseline-known model in which the observations of multiple epochs are incorporated, the ambiguities are assumed to be constant over time and the baseline components are assumed known. These corrected DD observations and the so estimated variances, will capture the combined effect of the transmitted signal quality, the receiver architecture like correlator and loops, as well as any remaining mis-modeled effects like multipath. The impact of multipath can be largely mitigated through the method explained in the following. Since the stations in use are static and their surrounding environment almost remains unchanged over time, the multipath influence on a signal of a specific frequency is expected

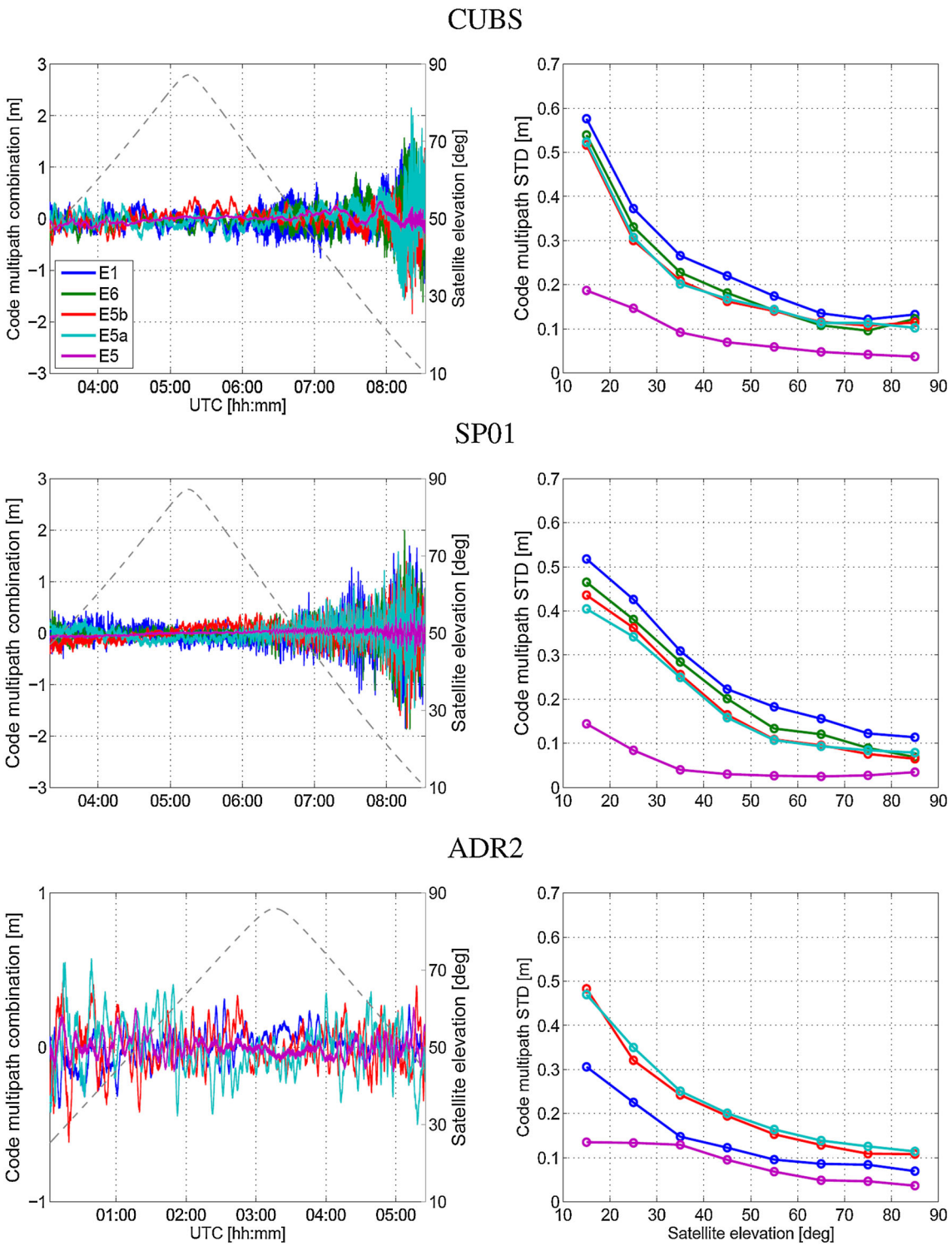

Fig. 3 Galileo code multipath behavior. (*Left*) code multipath combination time series based on the observations of station-satellite (from *top* to *bottom*) CUBS-E26 on DOY 118 of 2017, SP01-E26 on DOY 118 of 2017 and ADR2-E11 on DOY 21 of 2017. The satellite elevation is indicated by the dashed line. (*Right*) the standard deviation of the code multipath combination over elevation bins of 10°, based on all the Galileo observations recorded by (from *top* to *bottom*) station CUBS and SP01 during DOYs 118–127 of 2017 and station ADR2 during DOYs 12–21 of 2017

Table 3 LS-VCE estimation of the undifferenced code σ_p and phase σ_φ zenith-referenced standard deviations of the Galileo data

	Signal	CUBS-CUCS	CUBS-SP01	ADR2-APEL	CUBS-UWA0
σ_p (cm)	E1	21.2, 10.8	18.9, 9.8	17.5, 3.2	16.4, 9.8
	E5a	15.3, 5.6	14.9, 5.5	19.6, 3.7	13.7, 5.5
	E5b	16.3, 5.6	15.1, 5.6	18.8, 3.7	14.1, 5.6
	E5	6.4, 1.1	5.1, 1.1	6.8, 1.0	5.1, 1.2
	E6	16.5, 7.5	16.6, 7.6	–, –	13.1, 7.9
σ_φ (mm)	E1	1.4, 0.5	3.0, 0.8	3.8, 0.9	5.7, 3.2
	E5a	1.5, 0.5	3.1, 0.9	3.8, 1.3	6.8, 4.5
	E5b	1.4, 0.5	3.1, 0.8	3.6, 1.3	6.7, 4.4
	E5	1.1, 0.4	3.0, 0.8	3.6, 1.3	6.7, 4.4
	E6	1.4, 0.5	3.0, 0.8	–, –	5.6, 4.1

For each frequency and each baseline, two values are given for σ_p and σ_φ which, from left to right, correspond to the original and multipath-corrected data

to repeat when the Galileo receiver-satellite geometry repeats after 10 sidereal days. Therefore, by subtracting the corrected DD observations corresponding with the same satellite geometry (obtained every 10 sidereal days), the adverse multipath impact can be largely eliminated (Bock 1991; Genrich and Bock 1992; Zaminpardaz et al. 2016).

Table 3 lists the estimated standard deviations of the Galileo code σ_{p_j} and phase σ_{φ_j} observations with and without multipath corrections. For static stations, as used in this study, the multipath pattern for the Galileo constellation is expected to repeat every 10 sidereal days. This indicates that for every 10-day period, the multipath signature differs from day to day. Therefore, the standard deviations estimations of the original observations in Table 3 are obtained based on 10-day data sets. Prior to applying the multipath corrections to these data sets using the data of 10 days later as explained above, we first checked whether the multipath pattern indeed repeats after 10 sidereal days. Our observations showed that, in spite of the multipath environment remaining unchanged over time, for some of the satellites during some time intervals the multipath signature does not show a good repeatability. As an example, Fig. 4 for the station-satellite CUBS-E12 shows the E1 code multipath combination time series during a 48-min period on DOY pairs (blue-red) 123–133 (top) and 124–134 (bottom). The satellite elevations during the considered periods in top and bottom panels are similar. The UTC labels given in the top/bottom panel are on DOY 133/134, and therefore the UTC for the blue graphs are obtained by adding 2420 s ($\approx 10 \times 4$ min) to the shown UTC labels. It can be seen that while the multipath pattern shows consistent signature for DOY pair 123–133, its behavior differs from DOY 124 to DOY 134. A possible explanation for this discrepancy is as follows. The time shift that we use for DOY pairs 123–133 and 124–134 is

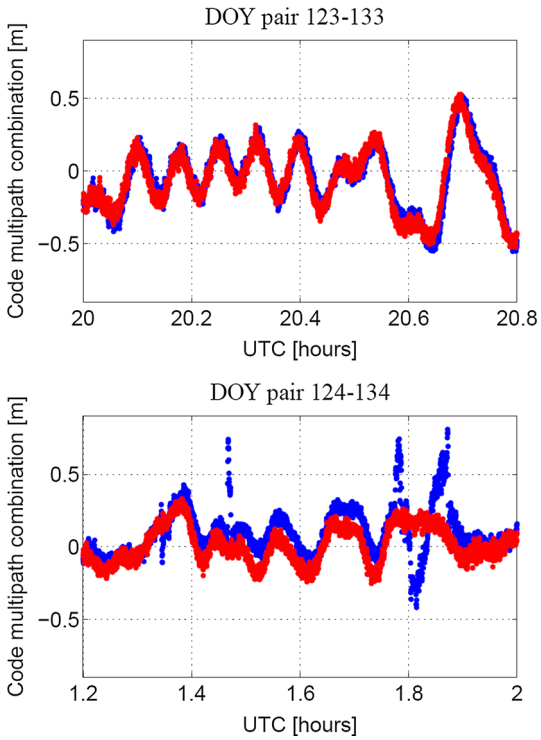

Fig. 4 Code multipath combination time series based on the E1 observations of station-satellite CUBS-E12 on (*top*) DOYs 123 (*blue*) and 133 (*red*) of 2017 (*bottom*) DOYs 124 (*blue*) and 134 (*red*) of 2017

2420 s which has been computed through cross-correlation of the corresponding baseline (CUBS-CUCS) estimation time series on DOYs 53 and 63 of 2017. However, our observations show that the repeat cycle varies among different Galileo satellites. Even for a given specific satellite, the repeat cycle changes from time to time. Any variation in the satellite geometry would then result in the variation in multipath signature. Thus, for estimating the multipath-corrected standard deviations in Table 3, we only chose

data of those days showing very similar multipath signature to that of their counterparts 10 days later, with the purpose of providing values one could achieve in case the multipath could have been eliminated. Note for multipath-corrected estimations, due to day-differencing, we have taken the doubling of the noise level into account through replacing w^s by $2w^s$.

Despite having the same receiver and antenna type, baselines CUBS-CUCS, CUBS-SP01 and CUBS-UWA0 show differences in their estimations of the original data standard deviations which can be attributed to the differences in the multipath environment of the stations CUCS, SP01 and UWA0. These discrepancies would vanish though, were the multipath effect be completely eliminated. This is also confirmed comparing the corresponding outcomes based on the original and multipath-corrected data. It can be seen that upon applying multipath corrections, the differences between the estimations of the mentioned three baselines get smaller. The stations forming the baseline ADR2-APEL have different antenna types (Table 2). The results presented in Table 3 for this station pair thus capture the combined effect of different antenna types involved. Comparing the standard deviation estimations of a specific signal based on the data of different baselines, one notes that the ordering would change if the multipath corrections are applied. For example, the code precision of the E5a original data improves from ADR2-APEL to CUBS-CUCS to CUBS-SP01 to CUBS-UWA0, whereas on the basis of E5a multipath-corrected data, the code precision improves from CUBS-CUCS to CUBS-SP01/CUBS-UWA0 to ADR2-APEL.

The order in which the signals can be arranged in terms of their precision is different for various receiver/antenna types. The code standard deviation of the E5 signal, however, shows lower dependency on the receiver/antenna type and the multipath environment, and significantly smaller values with respect to that of the other signals. Upon applying the multipath correction, the code standard deviations of all the signals experience a dramatic reduction which is a factor of five in the case of E5. The phase precision estimations either with or without multipath corrections, in contrast to their code counterparts, do not show any dependency on the signal type.

The results presented in Table 3 have been obtained combining the observations of the IOV and FOC satellites. We also carried out the LS-VCE estimations based on the IOV-only and FOC-only observations. The estimated code standard deviations of the FOC satellites are generally smaller than those of the IOV satellites. The phase observations of these two types of satellites, however, show similar precisions.

E5AltBOC RTK analysis

It was shown in the previous section that among the five Galileo signals, E5AltBOC shows a significantly higher signal power and lower level of multipath and noise. Such characteristics give us the motivation to further analyze the high-performance E5 signal for its potential capability in RTK positioning. In this section, we present the results of the Galileo E5-based instantaneous RTK performance. Our assessments are carried out based on the Galileo data collected by CUBS-CUCS (6-day data set; DOYs 54, 56–60 of 2017), CUBS-SP01 (5-day data set; DOYs 123–127 of 2017), ADR2-APEL (1-day data set; DOY 17 of 2017) and CUBS-UWA0 (2-day data set; DOYs 173–174 of 2017), once without multipath correction and once with multipath correction provided by the Galileo data 10 days later. With the current Galileo constellation, there exist time intervals with less than four visible satellites, accounting for 41 and 51% of a repeat cycle of 10 days at Perth and the Netherlands, respectively. These percentages increase further to 78% upon excluding E14 and E18, which is the case with our analyses in this contribution. The periods considered for our RTK evaluations accommodate time intervals with four to five visible satellites. In case of the first two baselines, there is a very short time interval with six satellites being visible. Given the limited number of visible Galileo satellites, the corresponding position dilution of precision (PDOP) reaches extremely large values, thus making positioning almost infeasible. In order to leave out these extreme values, in the sequel, we consider various PDOP thresholds when presenting RTK results.

GNSS single-frequency observational model

Let us assume that two receivers are simultaneously tracking m Galileo satellites on a single frequency, say E5. The corresponding multivariate DD observation equations can be cast in (Teunissen and Montenbruck 2017, Chap. 1; Hofmann-Wellenhof et al. 2008, Chap. 5)

$$E\begin{bmatrix} D_m^T p \\ D_m^T \varphi \end{bmatrix} = \begin{bmatrix} D_m^T G & 0 \\ D_m^T G & \lambda I_{m-1} \end{bmatrix} \begin{bmatrix} b \\ a \end{bmatrix}, \quad D\begin{bmatrix} D_m^T p \\ D_m^T \varphi \end{bmatrix} = \begin{bmatrix} \sigma_p^2 Q & 0 \\ 0 & \sigma_\varphi^2 Q \end{bmatrix}, \tag{4}$$

where $E[.]$ and D $[.]$ denote, respectively, the expectation and dispersion operator. The observations are formed by the vectors of the DD code and phase measurements, obtained by applying the between-satellite differencing operator D_m^T to the m-vector of between-receiver single-differenced (SD) code p and phase φ measurements. The $(m-1)\times m$ differencing operator can be formed as, e.g., $D_m^T = [-e_{m-1}, I_{m-1}]$ where e_{m-1} and I_{m-1} denote the

vector of ones and the identity matrix, respectively. The unknowns to be estimated are the 3-vector of the baseline increments b, linked to the observations through the $m \times 3$ geometry matrix G, and the $(m-1)$-vector of the DD ambiguities a, linked to the phase observations through the signal wavelength λ. The noise of the measurements is characterized through three factors, i.e., σ_p, σ_φ and $Q = 2 \times D_m^T W^{-1} D_m$. σ_p and σ_φ denote the zenith-referenced standard deviation of the undifferenced code and phase measurements (cf. 2), and W is the $m \times m$ diagonal matrix having the satellite elevation-dependent weights w^s (cf. 3) as its diagonal entries. Note our analyses are based on the short-baseline data where the differential ionospheric and tropospheric delays can be neglected.

As (4) suggests, for the single-epoch analyses, the phase observations are fully reserved for the estimation of the DD ambiguities. The estimation of the baseline would then be governed by the code observations only. The so obtained solutions for the baseline and the DD ambiguities are called float solutions. Upon resolving the DD ambiguities to their integer values, the phase observations would take the leading role in the baseline estimation. The so obtained solutions for the baseline and the DD ambiguities are called fixed solutions.

Ambiguity resolution results

Successful phase ambiguity resolution is a prerequisite to the realization of RTK positioning. As a measure to analyze the Galileo E5 ambiguity resolution performance in the framework of the model given in (4), we make use of the integer bootstrapped (IB) success rate as it is easy to compute, and also the sharpest lower bound to the integer least-squares (ILS) success rate which has the highest success rate of all admissible integer estimators (Teunissen 1999; Verhagen and Teunissen 2014). The formal IB success rate is computed as (Teunissen 1998)

$$\text{Formal IB Ps} = \prod_{i=1}^{m-1} \left[2\phi\left(\frac{1}{2\sigma_{\hat{z}_{i|I}}} \right) - 1 \right], \tag{5}$$

with $\phi(x) = \int_{-\infty}^{x} \frac{1}{\sqrt{2\pi}} \exp\{-\frac{1}{2}\upsilon^2\} \mathrm{d}\upsilon$ and $\sigma_{\hat{z}_{i|I}} (i = 1, \ldots, m-1$ and $I = 1, \ldots, i-1)$ being the conditional standard deviations of the decorrelated ambiguities. As the formal IB success rate is model-driven, to check the consistency between our data and the assumed underlying model, we also compute the empirical IB success rate which is data-driven and given as

$$\text{Empirical IB Ps} = \frac{\#\text{Correct fixed DD ambiguities}}{\#\text{Float DD ambiguities}}, \tag{6}$$

Table 4 Average single-epoch formal and empirical bootstrapped (IB) success rate (%), for the original and the multipath-corrected Galileo E5 data, collected by several baselines with the cutoff elevation of 10°

Baseline	PDOP < 30		PDOP < 20		PDOP < 10	
	emp	form	emp	form	emp	form
CUBS-CUCS	32.2	28.0	33.1	28.5	40.2	34.6
	95.2	92.1	95.5	92.3	97.6	95.0
CUBS-SP01	32.1	27.0	33.1	27.9	30.4	26.9
	89.6	93.0	89.7	93.4	87.3	94.2
ADR2-APEL	23.2	19.9	20.9	19.5	14.1	13.6
	95.6	93.7	95.2	93.7	96.9	91.0
CUBS-UWA0	29.3	29.5	29.2	29.8	27.0	29.4
	85.1	91.4	85.1	91.9	81.4	91.4

For each baseline and each PDOP threshold, two rows of values are given; the first row corresponds to original data, while the second row corresponds to the multipath-corrected data

emp empirical, *form* formal

To judge whether a float DD ambiguity $(\hat{a})$ is correctly fixed, its corresponding IB solution $(\check{a})$ is compared with the reference integer DD ambiguity (a) computed based on the multiepoch ILS solution of the baseline-known model. Table 4 shows the empirical and formal single-epoch IB success rates for both the original and multipath-corrected data of the mentioned four baselines. The formal values in this table are obtained through averaging the formal IB success rates over the period in use. In addition, since for the positioning results, coming in the next subsection, we consider various thresholds for PDOP value, we apply them here as well. One should, nevertheless, have in mind that the ambiguity resolution performance is not characterized through PDOP (Zaminpardaz et al. 2016, p. 546).

The results in Table 4 state that upon applying the multipath corrections, the IB success rates increase dramatically such that (almost) instantaneous ambiguity resolution becomes feasible. For example, if an ambiguity resolution success rate of 99.9% is sought for RTK positioning, our computation shows that, on average, four epochs of 1-s data are required. However, there still remains some inconsistencies between empirical and formal outcomes which can be attributed to the existence of the multipath residuals as explained in the following. As was mentioned previously, applying the multipath corrections cannot fully eliminate the multipath impact on our data sets, thereby leaving some residuals. The multipath-corrected standard deviations in Table 3, based on which the multipath-corrected formal success rates are computed, also, in turn, capture the impact of the multipath residuals

of the underlying data sets. The multipath-corrected empirical success rates in Table 4 are also affected by the multipath residuals of the corresponding data sets. The difference of the multipath residuals existing in the data sets used in Table 3 and those employed in Table 4, if non-negligible, can lead to disagreement between empirical and formal success rates. Note that the differences between the formal success rates of different baselines stem from the differences in the corresponding code/phase standard deviation (Table 3) and the satellite geometry.

Now, through visualization, we elaborate more on how applying the multipath correction improves the ambiguity resolution performance. For this purpose, we choose a period of 7000 s of the CUBS-CUCS data set, over which four Galileo satellites are visible from these stations, which in turn, results in three DD ambiguities. During this period, there was no loss of lock, and therefore the DD ambiguities remained constant. Figure 5 shows the corresponding three-dimensional scatter plot of the single-epoch solutions of $\hat{a} - a$ (gray) and $\check{a} - a$ (green: correctly fixed; red: wrongly fixed). While the left panel depicts the estimations based on the original data, the right panel shows those based on the multipath-corrected data. It can be seen that once the multipath corrections are applied to our data, the scatter plot of $\hat{a} - a$ shrinks considerably, and the number of incorrectly fixed solutions decreases from 29 to 3.

RTK positioning results

In this subsection, we discuss the single-epoch baseline estimation results based on the Galileo E5 observations. Setting the thresholds of 30, 20 and 10 for PDOP, Table 5 gives the empirical and formal single-epoch standard deviations of the estimated components of the baselines CUBS-CUCS, CUBS-SP01, ADR2-APEL, and CUBS-UWA0. The first two rows for each baseline give the ambiguity-float results on the basis of original and multipath-corrected data, respectively. The multipath-corrected results in Table 5 can be considered of practical relevance for kinematic users in a low multipath environment or for static baselines like, e.g., for deformation monitoring. As was shown in the previous subsection, the multipath-corrected Galileo E5 data can provide (almost) instantaneous successful ambiguity resolution. Therefore, the third row for each baseline gives the multipath-corrected ambiguity-fixed results, which are computed based on only the correctly fixed solutions. The formal and empirical standard deviations are computed on the basis of the respective formal and empirical variance matrix. The formal variance matrix is obtained from taking the average of all the single-epoch least-squares baseline variance matrices, whereas the empirical variance matrix is obtained from the differences of the estimates and the available ground truth of the mentioned baselines. Comparing the ambiguity-float results from the original data with those from the multipath-corrected data, the precision improvement achieved upon applying the multipath correction is a factor of about 4.24 which is the ratio of σ_p of the original data to $\sqrt{2} \times \sigma_p$ of the multipath-corrected data. The empirical results show consistency with the formal outcomes, particularly in case of the ambiguity-fixed scenario. Also, the positioning precisions depend on the receiver/antenna type as well as the extent to which the multipath impact can be mitigated (Table 3).

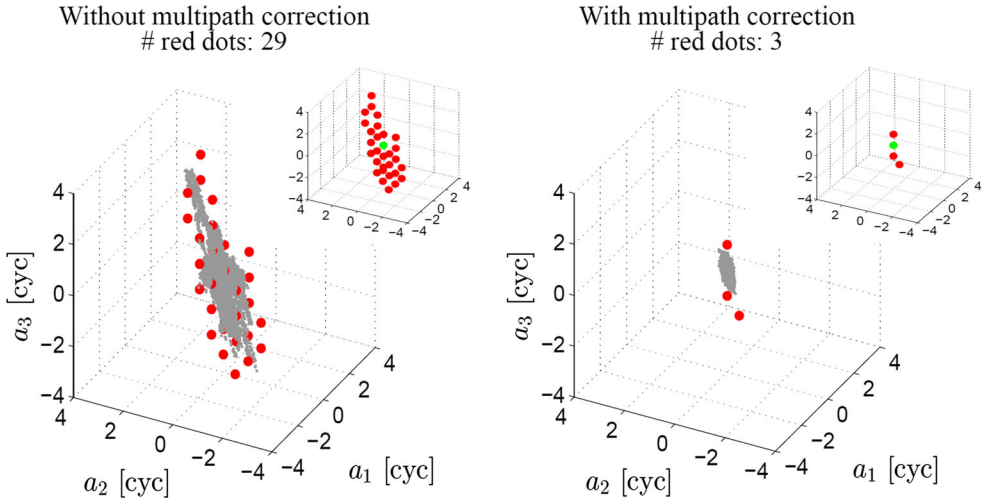

Fig. 5 Three-dimensional scatter plot of the single-epoch DD ambiguities in float mode $\hat{a} - a$ (*gray*) and fixed mode $\check{a} - a$ (*green* correctly fixed; *red* incorrectly fixed), corresponding with the Galileo E5 data collected by CUBS-CUCS over a period of 7000 s on DOY 54 of 2017. Given on *top* of *each panel* is the number of integers which were incorrectly determined by the IB estimator to be the DD ambiguities solution. Also, in the *upper right* of each panel, the *scatter plot* of only the fixed solutions is depicted. (*Left*) without multipath correction; (*right*) with multipath correction

Table 5 Single-epoch standard deviations of the estimated components of the baselines CUBS-CUCS, CUBS-SP01, ADR2-APEL and CUBS-UWA0 based on the Galileo E5 measurements collected with the cutoff angle of 10°

Baseline	PDOP < 30			PDOP < 20			PDOP < 10		
	North	East	Height	North	East	Height	North	East	Height
CUBS-CUCS									
	0.268, 0.305	0.225, 0.262	0.735, 0.804	0.235, 0.268	0.213, 0.238	0.593, 0.656	0.150, 0.165	0.185, 0.179	0.412, 0.423
	0.064, 0.076	0.044, 0.065	0.170, 0.201	0.053, 0.067	0.040, 0.059	0.143, 0.164	0.030, 0.041	0.034, 0.045	0.083, 0.106
	0.002, 0.003	0.002, 0.002	0.006, 0.007	0.002, 0.002	0.002, 0.002	0.005, 0.006	0.001, 0.001	0.002, 0.002	0.003, 0.004
CUBS-SP01									
	0.233, 0.260	0.197, 0.217	0.607, 0.662	0.200, 0.226	0.181, 0.191	0.505, 0.534	0.172, 0.168	0.165, 0.145	0.376, 0.339
	0.085, 0.077	0.071, 0.064	0.196, 0.196	0.077, 0.067	0.066, 0.056	0.158, 0.158	0.060, 0.050	0.060, 0.043	0.134, 0.100
	0.006, 0.006	0.005, 0.005	0.016, 0.015	0.004, 0.005	0.004, 0.004	0.012, 0.012	0.004, 0.004	0.003, 0.003	0.008, 0.008
ADR2-APEL									
	0.386, 0.387	0.226, 0.260	0.746, 0.799	0.397, 0.378	0.224, 0.248	0.715, 0.690	0.252, 0.305	0.225, 0.205	0.346, 0.503
	0.062, 0.081	0.051, 0.054	0.162, 0.167	0.062, 0.079	0.046, 0.052	0.143, 0.144	0.045, 0.063	0.035, 0.043	0.086, 0.105
	0.011, 0.010	0.006, 0.007	0.024, 0.022	0.010, 0.010	0.005, 0.006	0.019, 0.019	0.007, 0.008	0.003, 0.005	0.012, 0.014
CUBS-UWA0									
	0.229, 0.258	0.153, 0.170	0.614, 0.577	0.197, 0.224	0.143, 0.156	0.562, 0.511	0.166, 0.171	0.126, 0.138	0.364, 0.368
	0.071, 0.087	0.053, 0.058	0.180, 0.195	0.065, 0.076	0.050, 0.053	0.166, 0.173	0.052, 0.058	0.049, 0.047	0.125, 0.124
	0.029, 0.029	0.020, 0.019	0.070, 0.067	0.024, 0.025	0.018, 0.017	0.062, 0.060	0.017, 0.020	0.016, 0.015	0.050, 0.040

For each baseline and each PDOP threshold, six values per coordinate components are given on three rows. The first row contains the ambiguity-float results without multipath correction; the second contains the multipath-corrected ambiguity-float results and the third contains the multipath-corrected ambiguity-fixed results. On each row, from left to right, empirical and formal values are presented

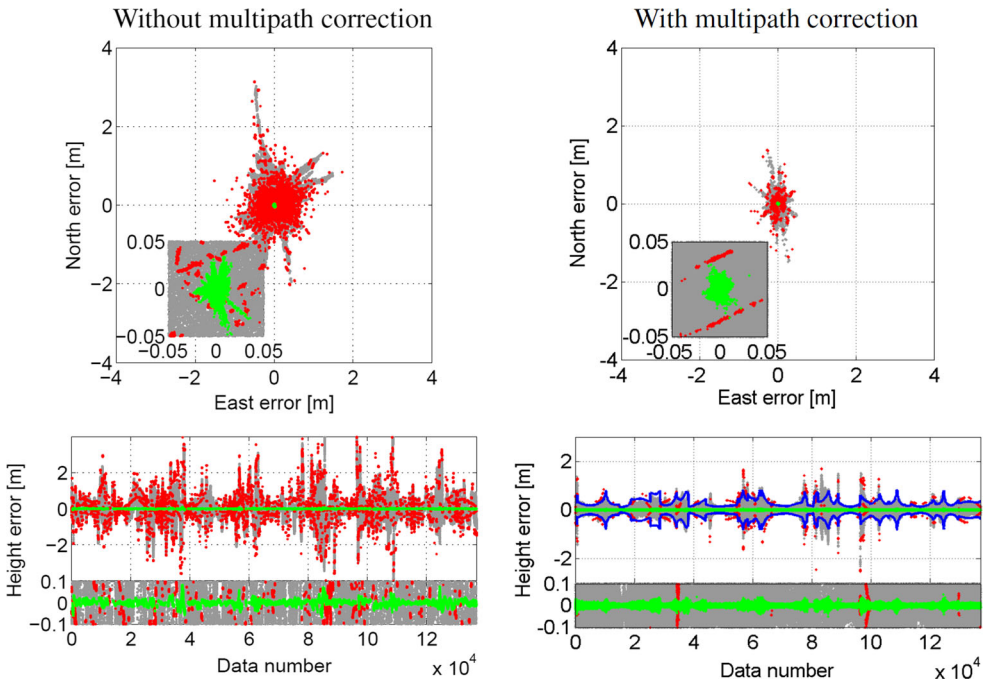

Fig. 6 CUBS-CUCS baseline solutions based on the Galileo E5 measurements collected on DOYs 54 and 56–60 of 2017 with the cutoff angle of 10°. These solutions correspond to PDOP values smaller than 30. (*Top*) *horizontal scatter plot* with a zoom-in in the lower left. (*Bottom*) height estimation errors time series with a zoom-in in the *bottom*. *Gray* float solutions; *green* correctly fixed solutions; *red* incorrectly fixed solutions. The *blue lines* in the *lower right panel* indicate the 95% formal confidence interval

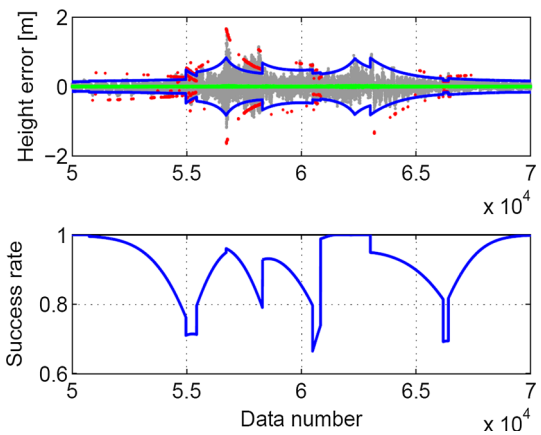

Fig. 7 Ambiguity resolution performance. (*Top*) a zoom-in of the height estimation errors time series illustrated in the *lower right panel* of Fig. 6. (*Bottom*) the corresponding time series of the single-epoch formal IB success rate

In the following, the positioning results of the baseline CUBS-CUCS are visualized and further discussed. Shown in Fig. 6 are the scatter plot of the CUBS-CUCS baseline horizontal components estimation errors (top) and the time series of the baseline height estimation error (bottom). Note, in this figure, we have stacked all the periods on DOYs 54 and 56–60 of 2017, during which a minimum of four Galileo satellites are visible, and the corresponding PDOP is less than 30. The estimation errors are computed by subtracting the baseline ground truth from the baseline single-epoch estimations. Different colors in this figure have the following meanings; gray: float solution, green: correctly fixed solution, and red: incorrectly fixed solution. The two left panels are based on the original data, whereas the two right panels correspond with the multipath-corrected data. In the lower right panel is also shown the 95% formal confidence interval (blue lines) based on the float height standard deviation. To obtain these results, a threshold of 30 was imposed on the PDOP.

In Fig. 6, the scatter plots do not show an ellipsoidal shape which is due to the significant changes that the receiver-satellite geometry undergoes during the mentioned six days. It can also be seen that the variation of the float solutions (gray) significantly decreases upon applying the multipath correction. This is due to the improvement of the E5 code precision following the elimination of the multipath effect from the code data (Table 3). The density of the red and green dots can be explained by means of the formal IB success rate. Figure 7 shows a zoom-in of the multipath-corrected height estimation error time series between (50,000, 70,000) (top) and the corresponding time series of the single-epoch formal IB success rate (bottom). The distribution of the red and green dots is in good agreement with the behavior of the formal IB success rate. When the success rate gets smaller, the density of red dots increases and vice versa.

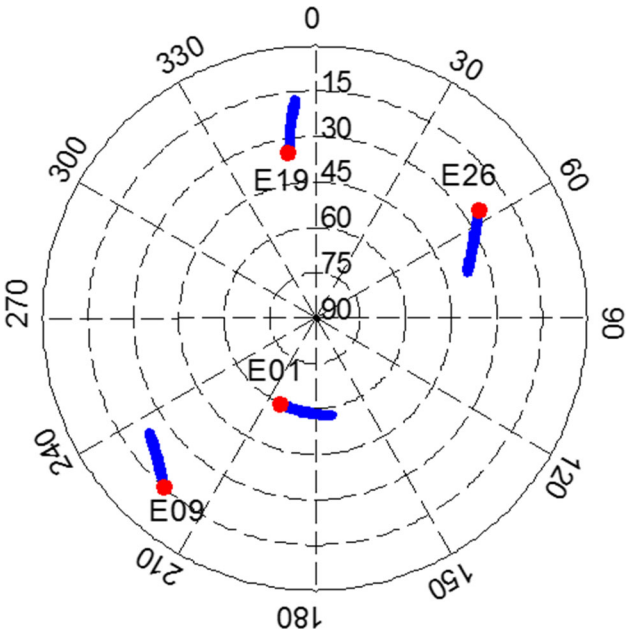

Fig. 8 Skyplot of Galileo at Perth, Australia, during UTC(18:35:11–19:21:51) on DOY 56 of 2017 with a cutoff elevation of 10°. The *red dots* show the location of the visible satellites at the first epoch of this time interval

The time series of the multipath-corrected height estimation errors, except for some intervals, shows a consistent signature with its formal counterpart (blue lines). The inconsistencies between the formal and empirical float solutions can be attributed to the fact that the multipath corrections that we apply to our data cannot eliminate the multipath effect completely. Instead, they capture largely the multipath trend (low-frequency multipath components) and partly the high-frequency multipath components which are of higher amplitudes in the satellite signals received at low elevations (Fig. 3, left).

Looking at the ambiguity-fixed solutions presented in the right panel of Fig. 6, during some time interval, different clusters of fixed solutions can be recognized, indicating that the DD ambiguities are resolved to different integer vectors during these periods. As an example, we consider the interval (30,200, 33,000) through which there exist three (two red and one green) clusters of fixed solutions, thus three different integer estimations of the ambiguities. Shown in Fig. 8 is the skyplot of the Galileo satellites at Perth during this period. According to this figure, four satellites are visible among which satellite E09 is just rising from the elevation of 15°. Figure 9 (right) shows the time series of the float and fixed DD ambiguities over the mentioned period, from top to bottom, for the satellite pairs E01–E09, E01–E19, and E01–E26, respectively. It can be seen that while the DD ambiguities of E01–E19 and E01–E26 are correctly fixed to 0, those corresponding with E01–E09 are varying between −1, 0 and 1 which is obviously due to the residuals of the high-frequency multipath components. Figure 9 (left) shows the three-dimensional scatter plot of the float DD ambiguities during the first 100 epochs of the interval (30,200, 33,000), where a_1: E01–E09, a_2: E01–E19 and a_3: E01–E26. The zero IB pull-in region (black parallelepiped), computed based on the average DD ambiguities variance matrix over the mentioned 100 epochs, is also illustrated in this figure. The ambiguities solutions inside the pull-in region are indicated by the green dots and those outside the pull-in region by the red dots. It can be seen that the scatter plot of the DD ambiguities deviates from the zero IB pull-in region along a_1 direction, corresponding with E01–E09.

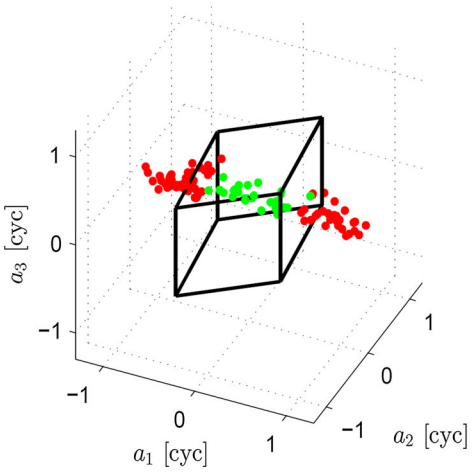

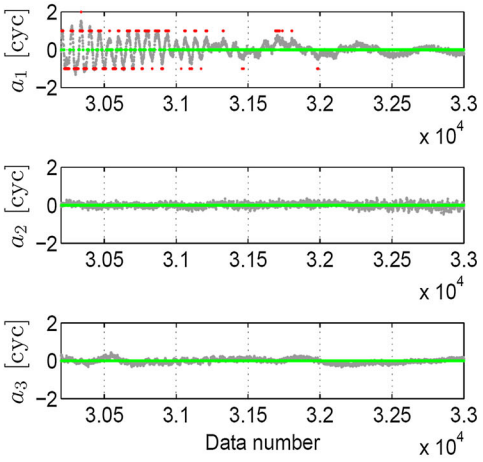

Fig. 9 (*Left*) Three-dimensional scatter plot of the float DD ambiguities corresponding with the satellite geometry shown in Fig. 8 during the interval (30200, 30300). The *black parallelepiped* is the IB pull-in region. The float DD ambiguities inside the IB pull-in regions are denoted by *green dots* and those outside the IB pull-in region by *red dots*. a_1: E01–E09, a_2: E01–E19 and a_3: E01–E26. (*Right*) time series of the float and fixed DD ambiguities over the mentioned interval. *Gray* float solutions; *green* correctly fixed solutions; *red* incorrectly fixed solutions

Summary and conclusion

We provided the results of the Galileo signals stochastic properties employing 1-s data collected by four short baselines of different lengths and receiver/antenna types. The assessments included the observations of both the IOV and FOC satellites in the constellation in April 2017 excluding E14 and E18. We analyzed the signal power, multipath performance and the noise level of the Galileo E1, E5a, E5b, E5 and E6 signals. The carrier-to-noise density ratio C/N0 measurements of the Galileo FOC satellites demonstrated higher values than those of the IOV satellites. This can be attributed to different transmit antenna patterns and transmit power levels of these two types of satellites, and also the signal power reduction of all the IOV satellites imposed by ESA in 2014. For two types of receiver/antenna in use, i.e., Septentrio PolaRx5/TRM 59800.00 SCIS (CUBS) and Leica GR50/LEI AR20 (ADR2), our C/N0 observations revealed the following ordering $E5 > E6 > E5b > E5a \approx E1$ and $E5 > E5b \approx E5a > E1$, respectively.

To analyze the multipath performance of the Galileo signals, the corresponding code multipath combinations were formed based on the observations of three stations (CUBS and SP01 at Perth and ADR2 in the Netherlands) with different multipath environment and receiver/antenna type. The standard deviations of the code multipath combination as a function of satellite elevation were illustrated. The multipath performance of three signals E5a, E5b and E6 were similar to each other, poorer than E1 in the case of station ADR2 and better than E1 in the case of stations CUBS and SP01. A strong satellite elevation dependency was visible in the code multipath of all these four signals. Taking considerably smaller values, E5 signal multipath showed a weak dependency on the satellite elevation.

Having investigated the multipath performance of the Galileo signals, we then turned our attention into the assessment of the measurement noise. To do so, we made use of the LS-VCE method to estimate the zenith-referenced variance of the signals on different frequencies. Our estimations are combinations of the transmitted signal quality, the receiver architecture including correlator and loops, and any remaining mis-modeled effects like multipath. Describing a multipath mitigation method, we presented the LS-VCE estimations of the mentioned variances for both the original and the multipath-corrected data of several short baselines of different lengths and receiver/antenna types. The order in which the signals can be arranged in terms of their precision is different for various receiver/antenna types. Upon applying the multipath correction, the code standard deviations of all the signals experienced a dramatic reduction. The code standard deviation of the E5 signal showed significantly smaller values with respect to that of the other signals, with low dependency on the receiver/antenna type and the multipath environment. Estimations based on the data of all four short baselines confirmed a standard deviation of about 6 cm without multipath correction and about 1 cm with multipath correction for the E5 code observations. The phase precision estimations either with or without multipath corrections did not show any dependency on the signal type.

Showing a significantly lower level of multipath and noise and higher signal power irrespective of the receiver/antenna type, E5 signal was further investigated for its capability in instantaneous RTK positioning. For this purpose, we made use of the observations recorded by all the mentioned baselines. It was shown that the Galileo E5 single-epoch ambiguity resolution IB success rate of about 90% is achievable for all the station pairs upon applying the multipath correction to the E5 data. This means that the Galileo E5 data, if corrected for the multipath effect, can make (almost) instantaneous ambiguity resolution feasible already based on the current constellation. The resultant ambiguity-fixed positioning precision varied as a function of the receiver/antenna type and the extent to which the multipath impact can be mitigated.

We showed that the multipath corrections, generated as described in this paper, capture largely the low-frequency multipath components and partly the high-frequency multipath components which are of higher amplitudes and mainly present in the satellite signals received at low elevations. Our results revealed that the residuals of these high-frequency multipath components after applying the multipath corrections can still lead to incorrect fixing of the DD ambiguities.

Acknowledgements The second author is the recipient of an Australian Research Council (ARC) Federation Fellowship (Project Number FF0883188). The Netherlands data were provided by Mr. Lennard Huisman from Kadaster, the Netherlands. This support is greatly acknowledged. We are also thankful to Dr. Nandakumaran Nadarajah and Dr. Mohammad Choudhury from Curtin University GNSS Research Center, Perth, Australia, for providing the data of UWA0 station.

References

Afifi A, El-Rabbany A (2014) Single frequency GPS/Galileo precise point positioning using un-differenced and between-satellite single difference measurements. GEOMATICA 68:195–205

Amiri-Simkooei AR, Teunissen PJG, Tiberius CCJM (2009) Application of least-squares variance component estimation to GPS observables. J Surv Eng 135(4):149–160

Bock Y (1991) Continuous monitoring of crustal deformation. GPS World 2(6):40–47

Cai C, Luo X, Liu Z, Xiao Q (2014) Galileo signal and positioning performance analysis based on four IOV satellites. Navigation 67:810–824

Cai C, Gao Y, Pan L, Zhu J (2015) Precise point positioning with quad-constellations: GPS, BeiDou, GLONASS and Galileo. Adv Space Res 56:133–143

Cai C, He C, Santerre R, Pan L, Cui X, Zhu J (2016) A comparative analysis of measurement noise and multipath for four constellations: GPS, BeiDou, GLONASS and Galileo. Surv Rev 48:287–295

de Bakker PF, van der Marel H, Tiberius CC (2009) Geometry-free undifferenced, single and double differenced analysis of single frequency GPS, EGNOS and GIOVE-A/B measurements. GPS Solut 13(4):305–314

de Bakker PF, Tiberius CC, Van Der Marel H, van Bree RJ (2012) Short and zero baseline analysis of GPS L1 C/A, L5Q, GIOVE E1B, and E5aQ signals. GPS solut 16(1):53–64

Diessongo TH, Schüler T, Junker S (2014) Precise position determination using a Galileo E5 single-frequency receiver. GPS Solut 18(1):73–83

EL-Hattab AI (2013) Influence of GPS antenna phase center variation on precise positioning. NRIAG J Astron Geophys 2:272–277

ESA (2016) Galileo fact sheet. http://esamultimedia.esa.int/docs/galileo/Galileo-factsheet-2016.pdf

Estey LH, Meertens CM (1999) TEQC: the multi-purpose toolkit for GPS/GLONASS data. GPS Solut 3(1):42–49

Euler HJ, Goad CC (1991) On optimal filtering of GPS dual frequency observations without using orbit information. Bull Geodes 65(2):130–143

European Union (2015) European GNSS (Galileo) open service signal in space interface control document, OS SIS ICD, Issue 1.2, Nov 2015

Gaglione S, Angrisano A, Castaldo G, Freda P, Gioia C, Innac A, Troisi S, Del Core G (2015) The first Galileo FOC satellites: from useless to essential. In: 2015 IEEE international on geoscience and remote sensing symposium (IGARSS), IEEE, pp 3667–3670. doi:10.1109/IGARSS.2015.732661814

Genrich JF, Bock Y (1992) Rapid resolution of crustal motion at short ranges with the global positioning system. J Geophys Res 97:3261–3269

Gioia C, Borio D, Angrisano A, Gaglione S, Fortuny-Guasch J (2015) A Galileo IOV assessment: measurement and position domain. GPS Solut 19:187–199

GSA (2017) Galileo programme. https://www.gsc-europa.eu/galileo-gsc-overview/programme

Guo F, Li X, Zhang X, Wang J (2017) Assessment of precise orbit and clock products for Galileo, BeiDou, and QZSS from IGS multi-GNSS experiment (MGEX). Surv Rev 21:279–290

Hauschild A, Montenbruck O, Sleewaegen JM, Huisman L, Teunissen PJ (2012) Characterization of compass M-1 signals. GPS Solut 16(1):117–126

Hellemans A (2014) A simple plumbing problem sent Galileo satellites into wrong orbits. http://spectrum.ieee.org/tech-talk/aerospace/satellites/a-simple-plumbing-problem-sent-galileo-satellites-into-wrong-orbits

Hofmann-Wellenhof B, Lichtenegger H, Wasle E (2008) GNSS-global navigation satellite systems, GPS, GLONASS, Galileo and more. Springer, Berlin

Langley R (2014) ESA discusses Galileo satellite power loss, upcoming launch. http://gpsworld.com/esa-discusses-galileo-satellite-power-loss-upcoming-launch/. Published 20 Aug 2014

Langley RB, Banville S, Steigenberger P (2012) First results: precise positioning with Galileo prototype satellites. GPS World 23:45–49

Li X, Ge M, Dai X, Ren X, Fritsche M, Wickert J, Schuh H (2015) Accuracy and reliability of multi-GNSS real-time precise positioning: GPS, GLONASS, BeiDou, and Galileo. J Geod 89:607–635

Liu T, Yuan Y, Zhang B, Wang N, Tan B, Chen Y (2017) Multi-GNSS precise point positioning (MGPPP) using raw observations. J Geod 91(3):253–268

Lou Y, Zheng F, Gu S, Wang C, Guo H, Feng Y (2016) Multi-GNSS precise point positioning with raw single-frequency and dual-frequency measurement models. GPS Solut 20:849–862

Mader G (2002) GPS antenna calibration at the national geodetic survey. National Geodetic Survey, NOS, NOAA, Silver Spring, MD

Nadarajah N, Teunissen PJG (2014) Instantaneous GPS/Galileo/QZSS/SBAS attitude determination: a single-frequency (L1/E1) robustness analysis under constrained environments. Navigation 61(1):65–75

Nadarajah N, Teunissen PJG, Raziq N (2013) Instantaneous GPS–Galileo attitude determination: single-frequency performance in satellite-deprived environments. IEEE Trans Veh Technol 62(7):2963–2976

Nadarajah N, Khodabandeh A, Teunissen PJG (2015) Assessing the IRNSS L5-signal in combination with GPS, Galileo, and QZSS L5/E5a-signals for positioning and navigation. GPS Solut 20(2):289–297

Odijk D, Teunissen PJG, Huisman L (2012) First results of mixed GPS + GIOVE single-frequency RTK in Australia. J Spat Sci 57(1):3–18

Odijk D, Teunissen PJG, Khodabandeh A (2014) Galileo IOV RTK positioning: standalone and combined with GPS. Surv Rev 46:267–277

Odolinski R, Odijk D, Teunissen PJG (2015) Combined BDS, Galileo, QZSS and GPS single-frequency RTK. GPS Solut 19:151–163

Pan L, Cai C, Santerre R, Zhang X (2017) Performance evaluation of single-frequency point positioning with GPS, GLONASS, BeiDou and Galileo. Surv Rev. doi:10.1080/00396265.2016.1151628

Simsky A, Sleewaegen JM, Hollreiser M, Crisci M (2006) Performance assessment of galileo ranging signals transmitted by GSTB-V2 satellites. In: Proceedings of ION GNSS 2006, Institute of Navigation, Fort Worth, TX, USA, 26–29 Sept, pp 1547–1559

Simsky A, Mertens D, Sleewaegen JM, Hollreiser M, Crisci M (2008a) Experimental results for the multipath performance of galileo signals transmitted by GIOVE—a satellite. Int J Navig Observ. doi:10.1155/2008/416380

Simsky A, Sleewaegen JM, Wilde WD, Hollreiser M, Crisci M (2008b) Multipath and tracking performance of galileo ranging signals transmitted by GIOVE-B. In: Proceedings of ION GNSS 2008, Institute of Navigation, Savannah, Georgia, USA, 16–19 Sept, pp 1525–1536

Steigenberger P, Montenbruck O (2016) Galileo status: orbits, clocks, and positioning. GPS Solut 21(2):319–331

Steigenberger P, Hugentobler U, Montenbruck O (2013) First demonstration of Galileo-only positioning. GPS World 24:14–15

Tegedor J, Øvstedal O, Vigen E (2014) Precise orbit determination and point positioning using GPS, Glonass, Galileo and BeiDou. J Geod Sci 4:65–73

Tegedor J, Øvstedal O, Vigen E (2015) Estimation of Galileo uncalibrated hardware delays for ambiguity-fixed precise point positioning. Navigation 63:173–179

Teunissen PJG (1998) Success probability of integer GPS ambiguity rounding and bootstrapping. J Geod 72(10):606–612

Teunissen PJG (1999) An optimality property of the integer least-squares estimator. J Geod 73(11):587–593

Teunissen PJG, Amiri-Simkooei AR (2008) Least-squares variance component estimation. J Geod 82(2):65–82

Teunissen PJG, Montenbruck O (eds) (2017) Springer handbook of global navigation satellite systems. Springer, Berlin

Tranquilla JM, Cam JP, Al-Rizzo HM (1994) Analysis of a choke ring groundplane for multipath control in global positioning system (GPS) applications. IEEE Trans Antennas Propag 42(7):905–911

Verhagen S, Teunissen PJG (2014) Ambiguity resolution performance with GPS and BeiDou for LEO formation flying. Adv Space Res 54(5):830–839

Zaminpardaz S, Teunissen PJG, Nadarajah N (2016) GLONASS CDMA L3 ambiguity resolution and positioning. GPS Solut 21(2):535–549

Safoora Zaminpardaz received her M.Sc. in Geodesy from University of Tehran. She has been pursuing her Ph.D. since July 2014 at the GNSS Research Centre, Curtin University, Australia. Her research interests include array-based multi-GNSS positioning, ionosphere sensing and integrity monitoring.

Peter J. G. Teunissen is professor of Geodesy and Navigation and Head of CUT's GNSS Research Centre. His current research focuses on multi-GNSS and the modeling of next-generation GNSS for high-precision positioning, navigation and timing applications.